



Spray Coating Experiments: Setups and Methodologies



**The latest eBook from
Advanced Optical Metrology.
Download for free.**

Spray Coating Experiments: Setups and Methodologies, is the third in our Thin Films eBook series. This publication provides an introduction to spray coating, three article digests from Wiley Online Library and the latest news about Evident's Image of the Year Award 2022.

Wiley in collaboration with Evident, are committed to bridging the gap between fundamental research and industrial applications in the field of optical metrology. We strive to do this by collecting and organizing existing information, making it more accessible and useful for researchers and practitioners alike.

EVIDENT
OLYMPUS

WILEY

Artificial Visual Systems With Tunable Photoconductivity Based on Organic Molecule-Nanowire Heterojunctions

Pengshan Xie, Xu Chen, Zixin Zeng, Wei Wang, You Meng, Zhengxun Lai, Quan Quan, Dengji Li, Weijun Wang, Xiuming Bu, Sai-Wing Tsang, SenPo Yip, Jia Sun,* and Johnny C. Ho*

The visual system, one of the most crucial units of the human perception system, combines the functions of multi-wavelength signal detection and data processing. Herein, the large-scale artificial synaptic device arrays based on the organic molecule-nanowire heterojunctions with tunable photoconductivity are proposed and demonstrated. The organic thin films of p-type 2,7-diocetyl[1]benzothieno[3,2-b][1] benzothiophene (C8-BTBT) or n-type phenyl-C₆₁-butyric acid methyl ester (PC₆₁BM) are used to wrap the InGaAs nanowire parallel arrays to configure two different type-I heterojunctions, respectively. Due to the difference in carrier injection, persistent negative photoconductivity (NPC) or positive photoconductivity (PPC) are achieved in these heterojunctions. The irradiation with different wavelengths (solar-blind to visible ranges) can stimulate the heterojunction devices, effectively mimicking the synaptic behaviors with two different photoconductivities. The long-term and multi-state light memory are also realized through synergistic photoelectric modulation. Notably, the arrays with different photoconductivities are adopted to build the hardware kernel for the visual system. Due to the tunable photoconductivity and response to multiple wavelengths, the recognition rate of neural networks can reach 100% with lower complexity and power consumption. Evidently, these photosynaptic devices are illustrated with retina-like behaviors and capabilities for large-area integration, which reveals their promising potential for artificial visual systems.

significantly to the recent development of the Internet of Things (IoT), artificial vision systems, unmanned driving, etc.^[1–3] In fact, the human brain, one of the most sophisticated structures in nature, can process and store large quantities of data simultaneously with high-speed and ultralow-power consumption.^[4,5] Inspired by the human brain, much progress with artificial synapse-based devices and systems has been achieved.^[6] Various intelligent sensory electronic devices, such as artificial throats, artificial skin, and artificial visual systems, are particularly focused.^[7–10] It is noted that ≈80% of the information is obtained by human vision; therefore, vision is the essential way to receive external signals.^[11,12] Also, the human visual system recognizes complex images of different wavelengths and converts optical signals into biological signals for processing, inspiring the development of artificial visual systems with optoelectronic devices.^[13] In this case, the artificial visual system has the potential to act as the signal receiver of bionic processors and artificial synapses.

It is known that neuronal electrical activity is the fundamental property of a visual system in the human brain, related to neuroplasticity.^[14] This neuroplasticity depends on the ability to process, maintain and inherit neurons based on the previous stimuli. Different from electrical signals,

1. Introduction

Since the advent of artificial intelligence, the evolution of information and communication technologies has contributed


P. Xie, Z. Zeng, W. Wang, Y. Meng, Z. Lai, Q. Quan, D. Li, W. Wang, X. Bu, S.-W. Tsang, J. C. Ho
Department of Materials Science and Engineering
City University of Hong Kong
Kowloon, Hong Kong SAR 999077, China
E-mail: johnnyho@cityu.edu.hk

X. Chen, J. Sun
Hunan Key Laboratory for Super-microstructure and Ultrafast Process
School of Physics and Electronics
Central South University
Changsha, Hunan 410083, China
E-mail: jiasun@csu.edu.cn

Y. Meng, J. C. Ho
State Key Laboratory of Terahertz and Millimeter Waves
City University of Hong Kong
Kowloon, Hong Kong SAR 999077, China

S. Yip, J. C. Ho
Institute for Materials Chemistry and Engineering
Kyushu University
Fukuoka 816–8580, Japan

J. C. Ho
Key Laboratory of Advanced Materials Processing & Mold
(Zhengzhou University)
Ministry of Education
Zhengzhou, Henan 450002, China

 The ORCID identification number(s) for the author(s) of this article can be found under <https://doi.org/10.1002/adfm.202209091>.

DOI: 10.1002/adfm.202209091

optical signals in human vision systems here have several advantages, including wide bandwidth, low power consumption, and long-distance transmission.^[15] Sun et al. applied SnO₂ nanowires (NWs) with ion gel to realize photo-synapses with the photoresponse in the solar-blind range.^[16] Subsequently, the In-Ga-Zn-O material was introduced with ion gel to fabricate the artificial vision system with a low back sweep subthreshold swing (< 60 mV per decade).^[17] In addition to introducing the dielectric layer, using heterojunction is also an effective method to realize the synaptic functions. Meng et al. introduced a 2D/0D hybrid structure to fabricate artificial synapses, where sub-femtojoule power consumption was realized by simply integrating black phosphorus quantum dots (QDs) onto 2D MoSSe.^[18] Similarly, Huang et al. dispersed CsPbBr₃ QDs into C8-BTBT/PS organic films for synaptic transistors, demonstrating ultra-low power consumption and effectively mimicking synaptic behaviors with response in the UV band.^[19] Moreover, various artificial visual systems with negative photoconductivity based on 2D materials and perovskites have been developed.^[1,20,21] On the one hand, to realize positive and negative photoconductivities in different wavelengths, heterojunctions stacked with multilayer 2D materials are commonly employed.^[22,23] A complex transfer process is then difficult to be avoided to configure these heterojunctions, while large-area heterojunction arrays are challenging to be achieved for practical utilization. On the other hand, perovskite materials are suitable for large-area fabrication but suffer from poor air stability. Due to the unique wide-range photoresponse, excellent electrical performance, robust stability, and, more importantly, the easy formation of large-scale arrays, III-V NW materials are anticipated to yield promising applications in artificial synaptic devices.^[24,25] Notably, the morphological and topological characteristics of these 1D NWs resemble the tubular axons, vital for efficient connections in the nervous system.^[26,27] In this regard, it is ideal to utilize III-V NW arrays integrated with other material systems, such as organic semiconductors, for heterojunctions in order to construct high-performance artificial visual systems.

In this work, we propose and demonstrate artificial photosynaptic devices based on organic molecule-nanowire heterojunctions. Specifically, the p-type organic semiconductor of 2,7-dioctyl[1]benzothieno[3,2-b][1] benzothiophene (C8-BTBT) or n-type organic material of phenyl-C₆₁-butyric acid methyl ester (PC₆₁BM) thin films were applied to wrap the indium gallium arsenide (InGaAs) NW arrays to configure two different type-I heterojunctions (i.e., p-n C8-BTBT/InGaAs or n-n PC₆₁BM/InGaAs), respectively. Because of the different major carriers in the two different organic materials, tunable photoconductivity could be achieved under irradiation stimuli from the UV to the visible range. It is revealed that the hole carriers of C8-BTBT or the electron carriers of PC₆₁BM would inject into InGaAs NWs under optical stimuli, which induced the persistent negative photoconductivity (NPC) or positive photoconductivity (PPC) accordingly. Owing to the high surface-to-volume ratio of InGaAs NWs, these two different heterojunctions can readily realize well-defined synaptic functions.^[28,29] It is remarkable that the short-term plasticity (STP), long-term memory (LTM), excitatory postsynaptic current (EPSC), inhibitory postsynaptic current (IPSC), and long-term potentiation/depression

(LTP/LTD) synaptic behaviors are reliably demonstrated with both visible and UV lasers, including the solar-blind range.^[30,31] In contrast to the single NW-based devices, the integration of printed NW arrays and solution-processed organic materials illustrate their great potential as active materials for large-area neural visual networks. A prototype of 4 × 4 artificial photosynaptic device arrays was demonstrated with optical memory function under the application of gate bias voltage (V_G). At the same time, the two photosynaptic devices with tunable photoconductivity (i.e., InGaAs/C8-BTBT for NPC and InGaAs/PC₆₁BM for PPC) were employed to construct the hardware kernel for simulating visual processing and recognition of the human eye. Different hardware kernels can detect various features in the image, such as the receptive field of the human retina. Then, these features were put into a neural network to classify 6 different letters with different colors. An impressive 100% classification accuracy was achieved, while only 51% was realized without hardware kernels. All these results evidently indicate the promising potential of these photosynaptic devices based on organic molecule-nanowire heterojunctions for practical utilization in artificial visual systems.

2. Results and Discussion

InGaAs NWs were synthesized through the two-step catalytic solid-source CVD method reported in previous works.^[28,32] The schematic illustration of the CVD setup for the NW synthesis is shown in Figure S1a (Supporting Information). **Figure 1a** depicts the schematic illustration of the artificial photosynaptic device configured with printed InGaAs NW arrays and top-wrapped organic semiconductor films. Scanning electron microscopy (SEM) was first adopted to assess the thickness, length, density, and surface condition of InGaAs NWs obtained by the two-step CVD method (Figure S1b,c, Supporting Information). Based on the transmission electron microscopy (TEM) images, spherical catalytic seeds are clearly observed at the NW tips (Figure S2a, Supporting Information), where this observation is consistent with the vapor-liquid-solid (VLS) growth mechanism typically known for InGaAs NWs.^[33,34] Obvious lattice fringes are witnessed by high-resolution TEM (HRTEM) with a spacing of 0.34 nm between adjacent lattice planes, corresponding to the <111> dominant direction of the InGaAs NWs (Figure 1b). Energy-dispersive X-ray spectroscopy (EDS) was then applied to evaluate the composition of the InGaAs NW, which confirmed the composition of In_xGa_{1-x}As with x being ≈0.49 (Figure S2b, Supporting Information). The corresponding elemental mappings were also obtained, demonstrating the homogenous distribution of In, As, and Ga along the NW body (Figure S3, Supporting Information). After material characterization, the NW printing process was used to fabricate large-scale InGaAs NW arrays.^[29] Then, photolithography was employed to define the channel region with 2 μm in length, and Ni was used as source/drain (S/D) metal contact electrodes, as presented in Figure 1c. C8-BTBT is an excellent p-type organic semiconductor widely used for high-performance field-effect transistors, artificial synapses, and phototransistors.^[35] The relatively wide band gap (≈3.8 eV) of C8-BTBT offers the ability to demonstrate good UV-responsive characteristics and

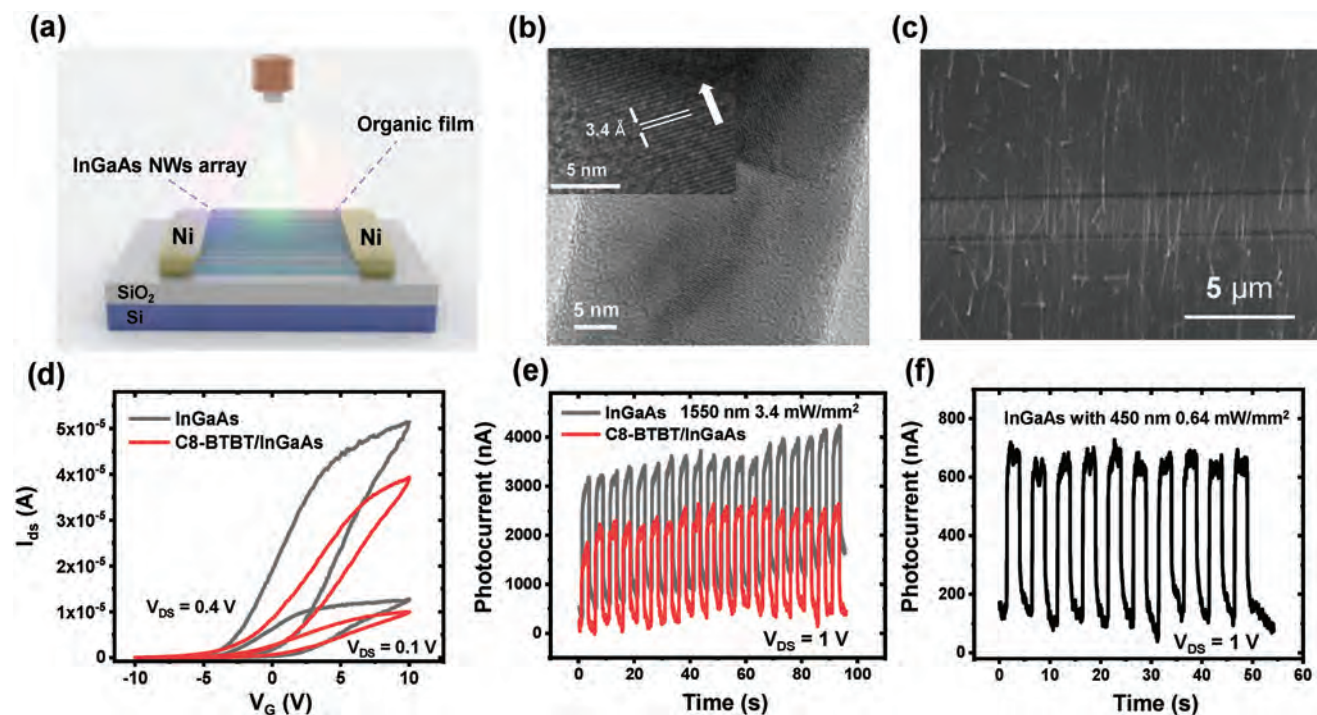


Figure 1. Characterization of the obtained InGaAs NWs and artificial photosynaptic devices. a) Schematic illustration of the photosynaptic device structure. b) HRTEM image of a typical InGaAs NW. The inset demonstrates the lattice spacing along the $\langle 111 \rangle$ direction of the NW. c) SEM image of the printed InGaAs NW arrays device. d) Transfer curves of the devices with and without C8-BTBT (1550 nm laser with a power density of 3.4 mW mm^{-2}). e) Photoresponse curves of the devices with and without C8-BTBT (1550 nm laser with a power density of 3.4 mW mm^{-2}). f) Photoresponse curves of the printed InGaAs NW arrays device (450 nm laser with the power density of 0.64 mW mm^{-2}).

potential applications with persistent photoconductivity.^[36–38] The molecular structure of C8-BTBT is displayed in Figure S4a (Supporting Information). Spin-coating was adopted to fabricate the C8-BTBT film top-wrapped onto the InGaAs NW arrays to construct the artificial photosynaptic device. Because of the band structure of type-I p-n heterojunction, the conduction band (CB) and valence band (VB) of InGaAs are completely covered by LUMO (lowest unoccupied molecular orbital) and HOMO (highest occupied molecular orbital) levels of C8-BTBT. The transfer curves of the devices with and without C8-BTBT are depicted in Figure 1d. The decrease of source/drain current (I_{ds}) (from $51 \mu\text{A}$ to $38 \mu\text{A}$) and the shift of threshold voltage (V_{th}) (from -3.5 V to -2 V) demonstrate that the holes, as the major carrier, injected from C8-BTBT would recombine with the electrons in InGaAs NWs. The output curves of the InGaAs/C8-BTBT device are shown in Figure S4b, which illustrates the effective V_G modulation and ohmic contact of the device. The photoresponse of the devices with and without C8-BTBT is shown in Figure 1e, which again indicates the reduced photocurrent in InGaAs/C8-BTBT device, consistent with the results of transfer curves. Typically, the InGaAs NWs have strong light absorption in the infrared band, but there is no photoresponse of C8-BTBT film in the same optical band. Therefore, both dark current and photocurrent of the device with organic molecule-nanowire heterojunctions decrease because of the carrier recombination that existed within the InGaAs NWs. It is noted that many intriguing photoelectric properties of 1D NWs are observed, where NPC is one of the most widely investigated phenomena.^[39,40] Due to the narrow band gap of InGaAs, when

the short wavelength laser with higher energy is applied, the induced photogenerated hot electrons would be trapped in the surface oxide, which serves as carrier scattering centers. Therefore, according to the thickness and density of the surface oxide layer, the InGaAs NWs devices would randomly show two different photoconductivities.^[41,42] The positive photoconductivity of the printed InGaAs NW arrays with 450 nm wavelength is demonstrated in Figure 1f. However, after integrating with the p-type organic semiconductor of C8-BTBT to construct type-I p-n heterojunction, the photoconductivity of the devices is unified to exhibit persistent NPC behavior. The NPC of the device with organic molecule-nanowire heterojunctions is depicted in Figure S4c (Supporting Information), while the corresponding NPC mechanism will be discussed later.

In biological synapses, the neurotransmitters are released by the presynaptic terminal when they receive external signals. The potential in the postsynaptic terminal would change according to the stimuli of neurotransmitters.^[43] Here, the stable and controllable persistent IPSC based on type-I p-n organic molecule-nanowire heterojunction demonstrates the potential of their use in artificial visual systems. To be specific, **Figure 2a** illustrates the schematic of a biological synapse. SEM and atomic force microscopy (AFM) are utilized to characterize the morphology of the C8-BTBT film covering the NWs (Figure S5, Supporting Information). The uniform distribution of S and C elements with a small surface roughness in the InGaAs/C8-BTBT overlap region demonstrates the high density and smoothness of the deposited organic film. Moreover, the SEM and optical images of the photosynaptic device are also

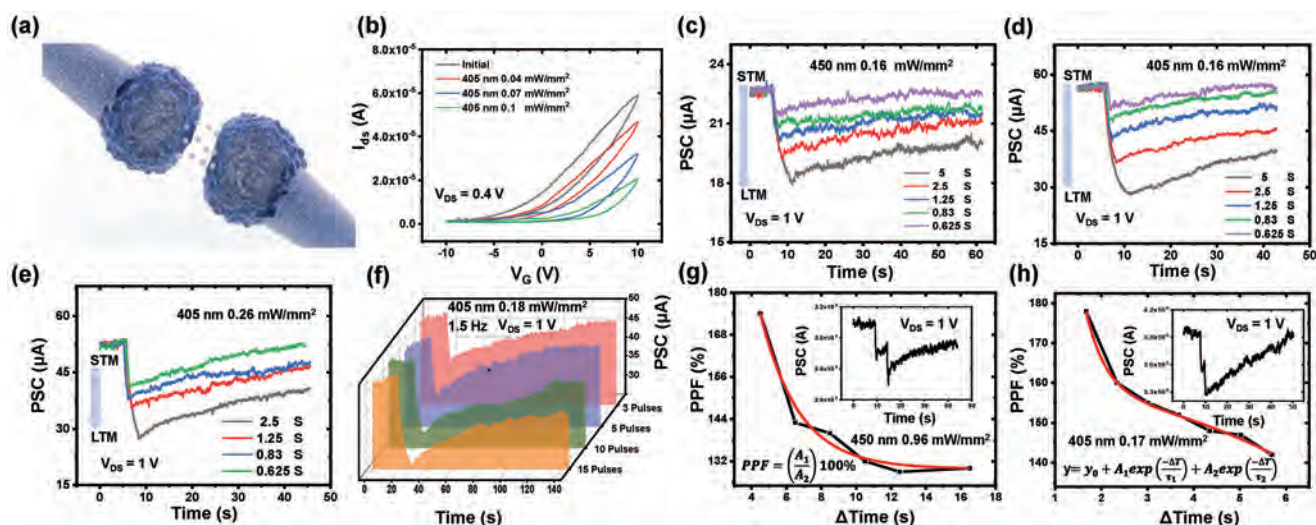


Figure 2. Synaptic behaviors mimicked by the artificial photosynapses configured with printed InGaAs NW arrays wrapped with the C8-BTBT film. a) Schematic illustration of the biological synapse. b) Transfer curves of the artificial photosynaptic device under 405 nm light irradiation with different power densities. c–e) IPSC behaviors of the artificial photosynaptic device under 450 nm and 405 nm light pulse with different pulse widths and fixed power density. f) IPSC behaviors of the artificial photosynaptic device with different numbers of 405 nm light pulses and fixed frequency (1.5 Hz). g, h) PPF index of the photosynaptic devices under two consecutive pulses with different intervals (450 and 405 nm, respectively). The insets are the corresponding curves with the highest PPF index value.

presented in Figures S6 and S7 (Supporting Information), respectively, again illustrating the good quality of the C8-BTBT film obtained. The transfer curves of the device with NPC characteristics under different power densities of 405 nm laser are shown in Figure 2b. It is obvious that the decrease in carrier concentration is amplified by the increasing irradiation intensity. The spike-intensity dependent plasticity (SIDP) and spike-time-interval-dependent plasticity of the photosynaptic device with 450 and 405 nm lasers are shown in Figure 2c–e, respectively. It is revealed that the value of IPSC is highly dependent on the wavelength, intensity, and duration of the laser irradiation. The two basic synaptic functions are categorized into short-term and long-term memory, demonstrating the ability to inherit and retain synaptic weights.^[44] Regardless of increasing the exposure time or laser intensity, the photosynaptic device displays the transformation from short-term to long-term memory (S/LTM). The photoresponse of the printed InGaAs NW arrays with 405 nm laser and the IPSC behaviors of the photosynaptic InGaAs/C8-BTBT device under 450 nm laser with different power densities are given in Figure S8 (Supporting Information). In addition, different numbers of 405 nm laser pulses are applied to the photosynaptic device to demonstrate the ability of weight inheritance (Figure 2f). It is unambiguous that with the increasing number of pulses, the LTM phenomenon gradually dominates and the photosynaptic device shows spike-number dependent plasticity (SNDP). Next, paired-pulse facilitation (PPF), one of the basic synaptic behaviors for decoding temporal information in neurobiology, is mimicked here with two different laser wavelengths.^[14] In this case, two consecutive presynaptic light spikes with different interspike intervals (Δ Time) are applied to mimic the PPF behavior in the photosynaptic device. Moreover, the PPF index can be defined by the ratio of the two different EPSC peaks (A_2/A_1).^[45] For 450 nm light pulses with an irradiation time of

0.5 s and light power density of 0.96 mW mm^{-2} (Figure 2g), when the Δ Time is 4.5 s, the maximum PPF index value is found to be 174%. The PPF of 450 nm light with different power densities and fixed Δ Time (3 s) are shown in Figure S9 (Supporting Information). Subsequently, similar to the 450 nm light, the PPF behavior is also successfully mimicked by 405 nm light pulses (Figure 2h). The maximum PPF index value is 178%, obtained at Δ Time = 1.67 s. The pulse interval-dependent decay of the PPF index with two different light pulses can be expressed utilizing a double exponential decay function as presented in the inset of Figure 2h.^[46] The y_0 parameter is the PPF index when the pulse interval approaches infinity. The t_1 and t_2 parameters are the decay constants of the rapid and slow phases, respectively. The A_1 and A_2 parameters are the initial facilitation magnitudes of the respective phases, accordingly. The t_1 and t_2 extracted from the equation with 450 and 405 nm light pulses are found to be 1.96 s and 2.39 s (Figure 2g), and 0.67 s and 0.83 s (Figure 2h), respectively. These results indicate that the PPF synaptic behaviors can be successfully mimicked by the organic molecule-nanowire photosynaptic device. Besides, the data about the PPF index of 405 and 450 nm light are shown in Figures S10 and S11 (Supporting Information).

The stable and persistent NPC phenomenon is achieved with the InGaAs/C8-BTBT heterojunction. Here, the synaptic behaviors with light pulses can also be mimicked by the photosynaptic device. In order to further study the NPC mechanism induced by the organic molecule-nanowire heterojunction, the photoluminescence (PL) spectra were collected to evaluate the carrier transfer of the heterojunction (Figure 3a). The C8-BTBT film was fabricated on the printed NW arrays by spin-coating with the same process. The PL spectra of C8-BTBT film and InGaAs/C8-BTBT heterojunction were measured under 320 nm laser excitation with the same power. It is obvious that

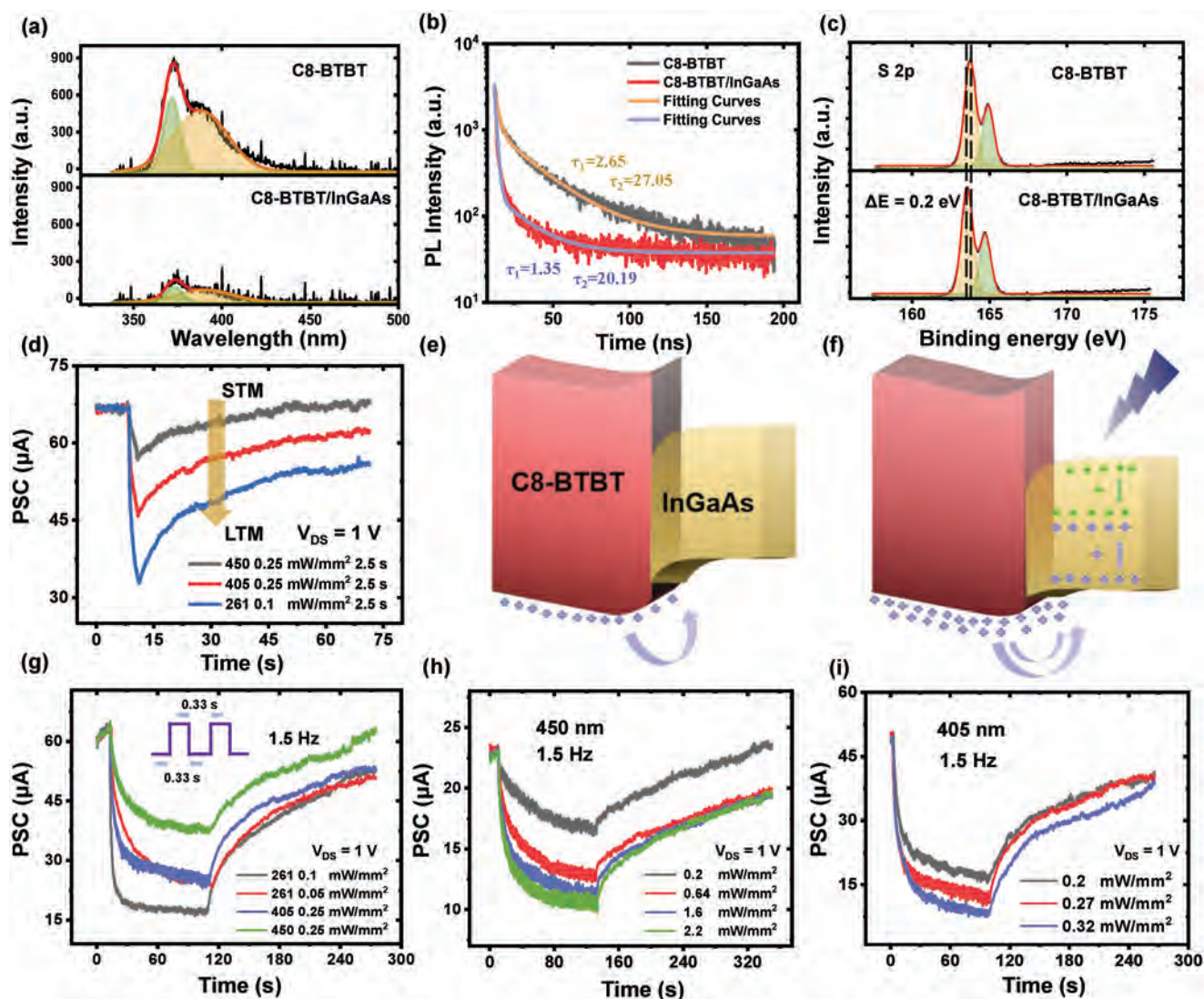


Figure 3. Mechanism of the persistent NPC phenomenon with type-I InGaAs/C8-BTBT heterojunction. a) PL spectra of the C8-BTBT film and InGaAs/C8-BTBT heterojunction. b) The corresponding time-resolved PL of the C8-BTBT film and InGaAs/C8-BTBT heterojunction. c) XPS of the C8-BTBT film and InGaAs/C8-BTBT heterojunction. d) IPSC behaviors of the artificial photosynthetic device with a single light pulse of different wavelengths. e) and f) Band structure of the InGaAs/C8-BTBT heterojunction before and after irradiation. g) LTP characteristics of the artificial photosynthetic device with light pulses of different wavelengths (1.5 Hz). h, i) LTP characteristics of the artificial photosynthetic device under 450 nm and 405 nm light pulses with different power densities.

the latter shows a six-fold intensity decrease of the emission peak at ≈ 372 nm compared with the former, which is similar to the heterostructures with photogenerated carrier transfer processes.^[47] Combined with the absorption of the C8-BTBT film (Figure S12, Supporting Information), the wide band gap of the C8-BTBT film is confirmed. Then, the time-resolved PL was assessed with data fitted by the bi-exponential function, revealing the shorter lifetime of the InGaAs/C8-BTBT heterojunction (Figure 3b).^[48] For the C8-BTBT film, the lifetimes of the fast and slow components are 2.65 ns and 27.05 ns, respectively, while those for the organic molecule-nanowire heterostructure decrease to 1.35 ns and 20.19 ns, accordingly. This significant decrease in the lifetime is attributed to the transfer of photogenerated carriers from the C8-BTBT to InGaAs NWs. X-ray photoelectron spectroscopy (XPS) was next employed to

investigate the carrier transfer characteristics of the InGaAs/C8-BTBT heterojunction (Figure 3c). Compared with the pristine C8-BTBT film, the S 2p peak of the heterojunction illustrates a slight shift of 0.2 eV toward the lower binding energy, confirming the existence of charge carrier transfer at the organic molecule-nanowire interface.^[49] Figure 3d demonstrates the IPSC behaviors with light pulses of different wavelengths. It is interesting that the stronger IPSC effect is obtained with light pulses of the shorter wavelength, even at the weaker light power (i.e., 261 nm). In order to explain the charge carrier transfer and NPC phenomenon, the band structures of the organic molecule-nanowire heterojunction before and after applying light pulses are compiled in Figure 3e,f. In this work, UV photoelectron spectroscopy (UPS) and absorption spectroscopy are employed to assess the band structure of

$\text{In}_{0.48}\text{Ga}_{0.52}\text{As}$ NWs (Figures S13 and S14, Supporting Information). The band gap and Fermi level extracted from Figures S13 and S14 (Supporting Information) are 0.84 eV and -4.17 eV, respectively. This way, when $\text{In}_{0.48}\text{Ga}_{0.52}\text{As}$ NWs and C8-BTBT are in contact, there is confirmed to have a type-I heterojunction. Due to the difference in Fermi level, a built-in electric field would be developed at the InGaAs-C8-BTBT interface, resulting in the band bending without applying light pulses (Figure 3e). This prediction is consistent with the results of XPS.^[49,50] Also, the p-type C8-BTBT film has holes as the major charge carrier, which would transfer into the InGaAs NWs to suppress the current, as shown in Figures 1d,e. Moreover, because of the relatively large gap and energy barrier between the LUMO level of C8-BTBT (-1.8 eV) and CB of InGaAs, the electrons transfer from C8-BTBT to InGaAs NWs is more difficult than holes.^[51] At the same time, C8-BTBT has a stronger absorption in the UV range (Figure S12, Supporting Information). When light pulses of shorter wavelengths are irradiated at the heterojunction, more photogenerated holes in C8-BTBT are injected into the NWs due to the built-in electric field at the InGaAs-C8-BTBT interface (Figure 3f). Injected holes would recombine with the electrons in NWs and induce the NPC phenomena.^[22,52] Since InGaAs NWs have the photoresponse in the infrared range, 1550 nm light is used to investigate the carrier recombination of the heterojunction after using visible light pulses. Figure S15a (Supporting Information) demonstrates the transfer curves after 450 nm and 1550 nm light irradiation. After 450 nm light (10 s, 2.2 mW mm⁻²) irradiation, the decrease of the current indicates the recombination of electrons into the NWs. Subsequently, the infrared irradiation induces photocarriers in the NWs without influence in C8-BTBT, making the transfer curves recover toward the initial state. In Figure S15b (Supporting Information), two different wavelength lights were applied to the heterojunction simultaneously after an infrared pulse (2.7 mW mm⁻², 5 s). Because infrared excitation and carrier recombination exist simultaneously, the different photocurrents can be controlled by the power density of 405 nm light. As discussed above, the persistent IPSC of the artificial photosynaptic device is highly dependent on the light power and wavelength, which shows similar functions to human eyes. The LTP characteristics of the artificial photosynaptic organic molecule-nanowire heterojunction device induced by persistent IPSC are displayed in Figure 3(g-i). The different wavelength light pulses are utilized to induce different levels of LTP characteristics (Figure 3g). It is noted that solar-blind light (261 nm) can realize strong LTP characteristics even with very weak light. The pulses' power within the UV and visible range can also modulate the weight changes in LTP characteristics (Figure 3h,i). Therefore, the number of photogenerated holes in C8-BTBT varies with the laser power, wavelength range, and pulse numbers. When a weak light pulse with short irradiation time is applied, only a small amount of photogenerated holes can enter the nanowire, which would cause the STM characteristics. As the laser intensity and duration increase, more photogenerated holes will enter the nanowire, resulting in more recombination and causing LTM characteristics. Besides that, in order to further verify the mechanism of the NPC phenomenon, the gallium antimonide (GaSb), as a p-type NW, was applied to fabricate the p-p heterojunction with C8-BTBT. The printing

GaSb arrays and C8-BTBT film were fabricated with the same process. Interestingly, this p-P heterojunction would not have the NPC phenomenon. On the contrary, the strong positive photoconductivity would be realized with 405 and 450 nm laser pulses as shown in Figure S16 (Supporting Information). This result shows that injecting the same type of charge carriers does not induce NPC.

Apart from injecting heterogeneous carriers into the InGaAs/C8-BTBT heterojunction for persistent NPC phenomena, PC₆₁BM, another popular organic material widely used in solar cells, is as well introduced to construct the type-I n-n InGaAs/PC₆₁BM heterojunction.^[53,54] The SEM images and EDS analysis of the fabricated device are shown in Figure S17 (Supporting Information). The molecular structure, optical images, and AFM analysis of PC₆₁BM covering the printed InGaAs NW arrays are compiled in Figure S18 (Supporting Information). It is evident that the deposited PC₆₁BM film is conformal and dense without any obvious pinholes, with constituent elements uniformly distributed. This observation demonstrates the high quality of the deposited film, which is essential for constructing the high-quality heterojunction. Also, the PPC phenomenon can be successfully realized by the InGaAs/PC₆₁BM heterojunction, which illustrates the potential of building artificial visual systems with positive photocurrent. The LTP characteristics and EPSC behaviors with light pulses of 405 nm irradiation are shown in Figure 4a,b. The artificial photosynaptic devices based on these n-n heterojunction yield good weight inheritance and preservation behaviors in LTP characteristics under successive 405 nm and 450 nm irradiation with different power densities (Figure 4a,d). The spike-time-interval-dependent plasticity of 405 nm (0.13 mW mm⁻²) and 450 nm (0.14 mW mm⁻²) irradiation with different duration times are investigated in Figure 4b,e. Furthermore, the 3, 5, and 10 pulses with 405 nm (0.13 mW mm⁻²) and 450 nm (0.14 mW mm⁻²) lasers are shown in Figure 4c,f and show the SNDP characteristic. The transformation from STM to LTM can be simply achieved by modulating the irradiation time and pulse numbers. Similar to the InGaAs/C8-BTBT heterojunction, the artificial photosynapse with the n-n InGaAs/PC₆₁BM heterojunction can as well mimic the synaptic behaviors successfully. Moreover, the EPSC behavior is also highly sensitive to the irradiation wavelengths, power densities, and pulse numbers. The laser pulses with shorter wavelengths are easier to induce higher EPSC, demonstrating the potential for visual and color recognition. The absorption spectrum of PC₆₁BM and the band structure of InGaAs/PC₆₁BM heterojunction are depicted in Figure S19 (Supporting Information), which illustrates the different mechanisms of PPC here.^[55,56] Explicitly, the photogenerated electrons in PC₆₁BM would first inject into the InGaAs NWs under laser pulses. Then, the type-I heterojunction prevents the reflux of the electrons. Besides, due to the relatively large gap between the HOMO level of PC₆₁BM (-6.1 eV) and VB of InGaAs, the transfer of holes from PC₆₁BM to InGaAs NWs is difficult. Hence, more photogenerated electrons would inject into the NWs than the hole counterparts, inducing the PPC phenomenon. PL and time-resolved PL spectra were collected for the InGaAs/PC₆₁BM heterojunction to evaluate and confirm the charge carrier transfer under laser irradiation (Figure S20, Supporting Information). The

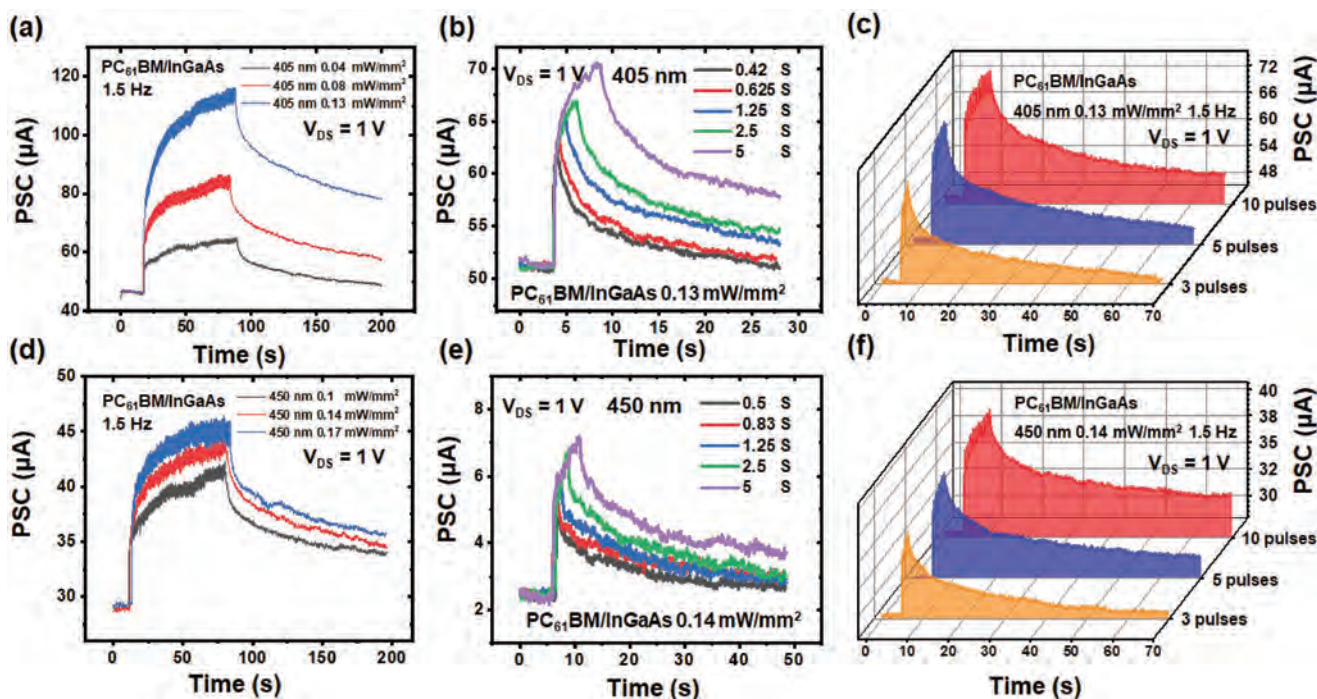


Figure 4. Synaptic behaviors mimicked by the artificial photosynapses configured with printed InGaAs NW arrays wrapped with the PC₆₁BM film. LTP characteristics of the artificial photosynaptic device under a) 405 nm and d) 450 nm light pulses with different power densities (1.5 Hz). EPSC behaviors of the synaptic device under b) 405 nm and e) 450 nm light pulses with different pulse widths. EPSC behaviors of the synaptic device with different numbers of c) 405 nm and f) 450 nm light pulses and the fixed frequency (1.5 Hz).

PPF effect as a basic synaptic characteristic is also mimicked successfully based on the photosynaptic InGaAs/PC₆₁BM device. The two consecutive pulses of 405 nm (0.33 s, 0.14 mW mm⁻²) and 450 nm (0.33 s, 0.17 mW mm⁻²) irradiation with the fixed duration time and power density were applied with the responses presented in Figures S21 and S22 (Supporting Information), respectively. For the 405 nm laser, when ΔTime is 1 s, the maximum PPF index value is found to be 130%, and the t_1 and t_2 values extracted from the double exponential decay function in Figure 2h are 0.88 s and 3.11 s, accordingly (Figure S21a, Supporting Information).^[46] Subsequently, similar to 405 nm laser, the maximum PPF value obtained by 450 nm laser pulses is 133% with ΔTime of 1 s. The t_1 and t_2 values are found to be 0.39 s and 2.69 s obtained from the same double exponential decay function (Figure S22a, Supporting Information). Moreover, because of the relatively wide absorption range of PC₆₁BM, the 261 nm and 532 nm wavelength lasers were adopted to induce LTP characteristics with the PC₆₁BM/InGaAs photosynaptic device (Figure S23a,b, Supporting Information). Besides that, SNDP is also realized by a different number of 532 nm laser pulses, as shown in Figure S23c (Supporting Information). In this case, the heterojunction devices can effectively mimic a series of synaptic behaviors, revealing their great capabilities in constructing high-performance artificial visual systems composed of positive and negative photoconductors. In order to show the potential for practical applications, the air stability of two photosynaptic devices was investigated and shown in Figure S24 (Supporting Information). The devices were put into a moisture-proof box with a fixed humidity of

40% in air atmosphere and tested with the LTP characteristics. As shown in Figure S24a (Supporting Information), for the device based on C8-BTBT/InGaAs NWs, the PSC decreases 5.6% (3 days) and 18.5% (7 days) with 405 nm light pulses, respectively. Moreover, the air stability of photosynaptic devices with PC₆₁BM/InGaAs NWs is shown in Figure S24b (Supporting Information). The PSC decreases by 18.1% (3 days) and 33.3% (7 days) with 60 blue light pulses, accordingly.

In this work, both NPC and PPC phenomena can be observed by controllably injecting different photogenerated charge carriers into the two different heterojunctions. For the InGaAs/C8-BTBT heterojunction photosynaptic device, the holes injected from C8-BTBT under laser irradiation would cause carrier recombination in the NWs. Furthermore, the V_G bias can be introduced to investigate the memory characteristics of these artificial photosynaptic devices. When the large positive V_G (40 V) is applied to the gate, there are large numbers of electrons accumulated in the NW channel.^[21,52,57] Once the 405 nm laser (1.1 mW mm⁻², 5 s) is irradiated onto the device, the PSC value would drop as expected. However, since the channel is already accumulated with electrons before irradiation, generating substantial additional amounts of electrons in the channel is not accessible after recombination. This way, the current of the synaptic device can maintain at a low level for a relatively long time. Figure 5a shows the synergistic photoelectric modulation for long-time memory (> 10⁴ s). The relaxation time fitted with the Kohlrausch stretched exponential function demonstrates that the memory loss here is also consistent with the situation in biological systems (Figure 5b).^[12,14,58]

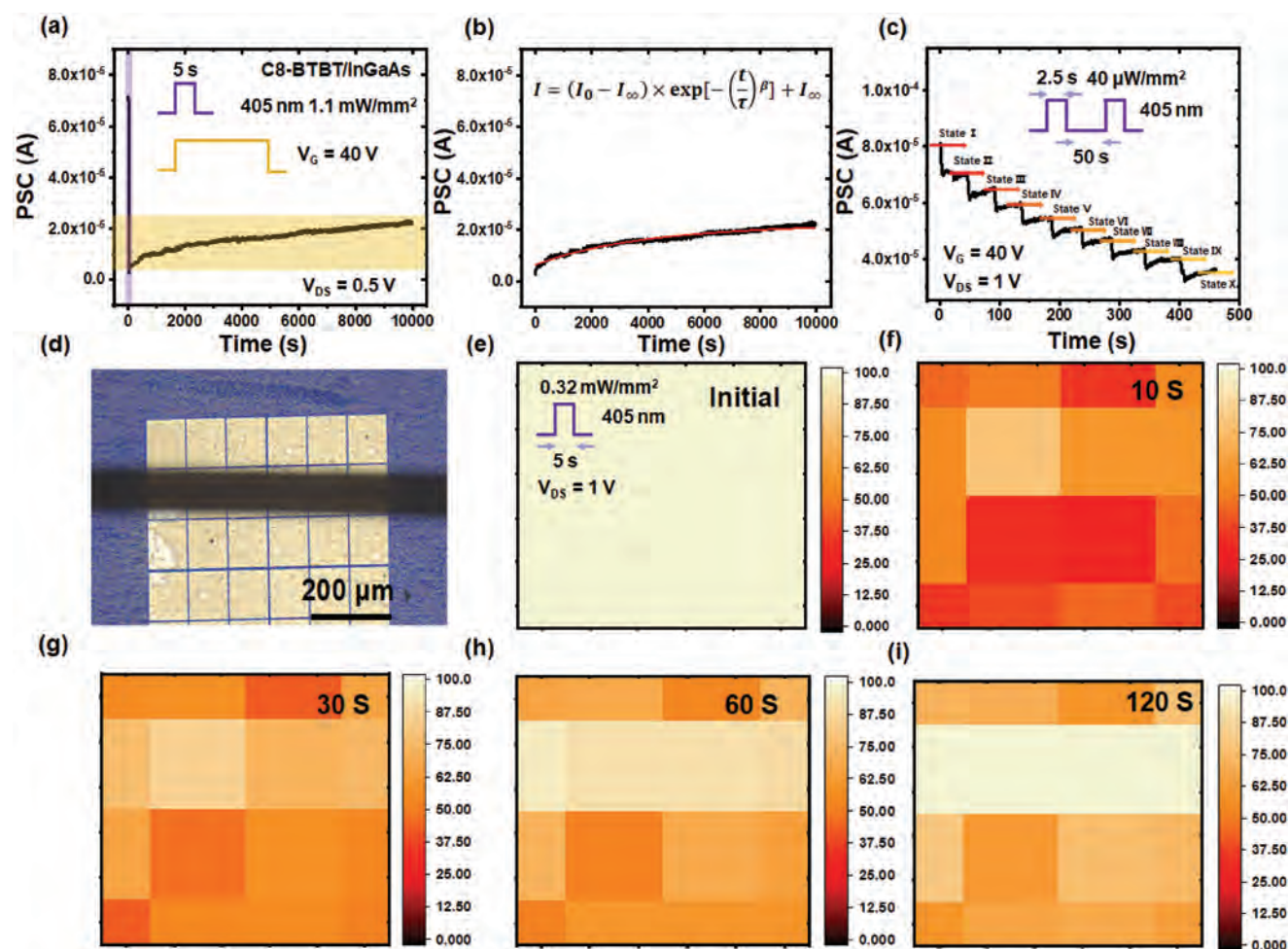


Figure 5. Optical memory function realized with the artificial photosynaptic device arrays. a) Synergistic photoelectric modulation for long-time memory with InGaAs/C8-BTBT heterojunction device. b) Corresponding relaxation time fitted with the Kohlrausch stretched exponential function. c) Different memory states configured with the NPC phenomenon. d) Optical image of the 4×4 arrays based on InGaAs/C8-BTBT heterojunction devices and the human hair is used to block the laser irradiation. e–i) The percentage change of EPSC after a single 405 nm pulse irradiation.

The different memory states are as well tested and shown in Figure 5c. Under the synergistic photoelectric modulation, the weak 405 nm laser ($40 \mu\text{W mm}^{-2}$) can realize more than eight memory states in the photosynaptic InGaAs/C8-BTBT device, which show the potential in achieving over 3 bits (8 distinguishable levels) memory function.^[59,60] Moreover, the 261 nm and 532 nm laser stimuli are applied to the InGaAs/C8-BTBT and InGaAs/PC₆₁BM heterojunction devices, respectively, to achieve the LTM function with synergistic photoelectric modulation (Figure S25, Supporting Information). For human visual systems, millions of nerve fibers transfer data to the brain for various processing. In this case, device integrability and scalability are indispensable for artificial visual systems. The printable NW arrays combined with the solution-processable organic thin films are suitable for this large-area fabrication, which can overcome the shortcomings of being difficult to integrate heterojunction devices on a large scale. Besides, lithography techniques, such as photolithography, can be used to fabricate the device arrays with high density. Hence, the 4×4 array based on photosynaptic InGaAs/C8-BTBT devices are

fabricated in this study, and a human hair was utilized to create a pattern for laser irradiation onto the device array (Figure 5d).^[61] The 405 nm laser pulse was then applied, and the percentage change of output current is shown in Figure 5(e–i). Because of the light blocking, the covered devices give faster current recovery. As shown in Figure 5i, the location covered by the hair can still be identified 120 s after irradiation.

More importantly, the two different photosynaptic devices with negative and positive photoconductivities (i.e., InGaAs/C8-BTBT and InGaAs/PC₆₁BM) were used to build an array to define the hardware kernel. The photoresponse characteristics of these synaptic devices to different irradiation power densities and wavelengths (i.e., red, green, and blue regimes) are utilized to simulate the visual processing and recognition functions of the human eye, as shown in Figures S26 and S27 (Supporting Information).^[62] The key role of the receptive field on the human retina is to speed up visual perception in the brain by extracting its key features to process visual information early (Figure 6a). Using this principle, we can extract key features of the image by the 3×3 hardware kernels, and

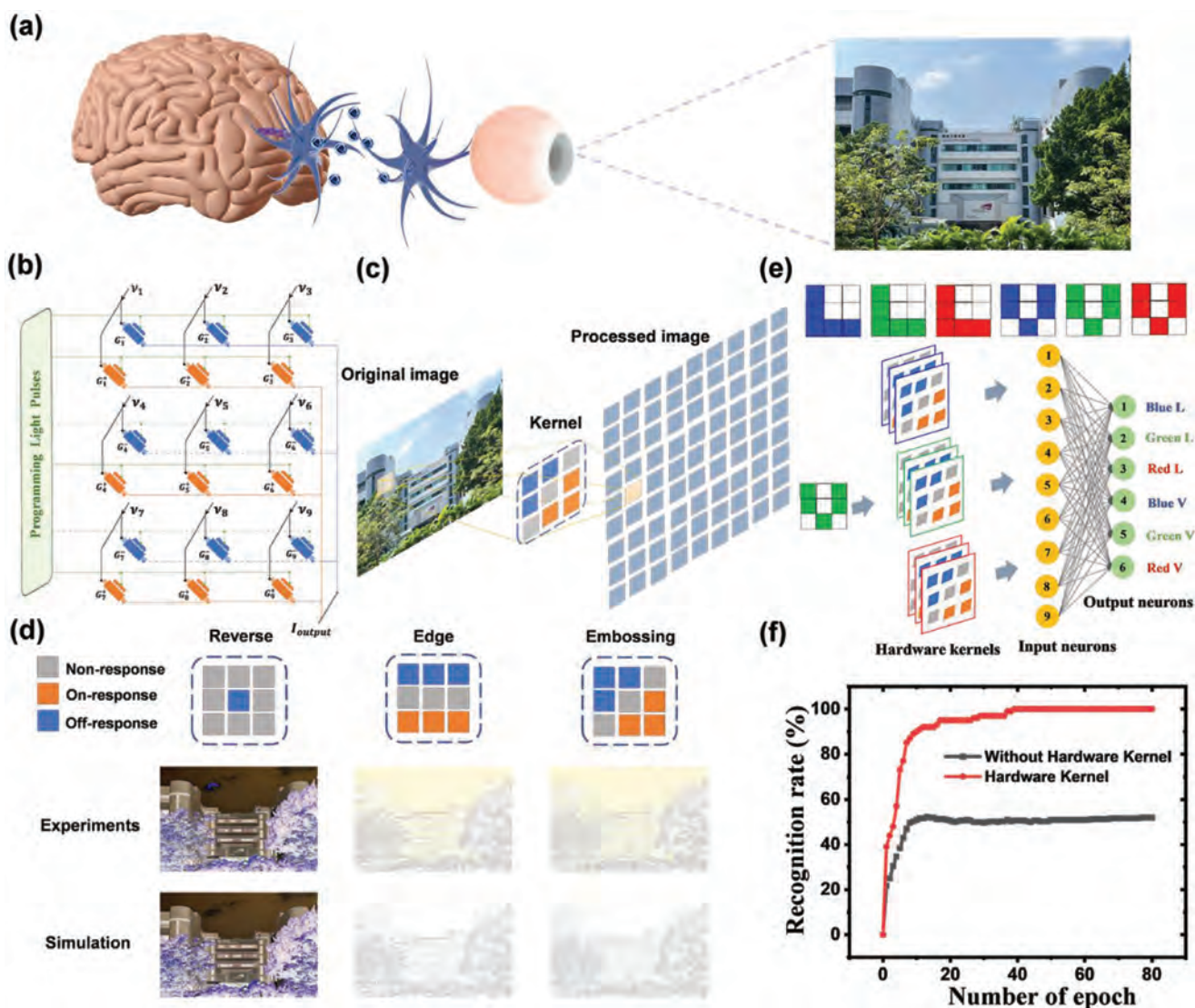


Figure 6. The hardware kernel for simulating the visual processing and recognition functions of the human eye based on NPC and PPC devices. a) Schematic illustration of the human visual system. b) Demonstration of the kernel array network. c) Functions of visual processing based on the hardware kernel. d) Experimental and simulation results of the hardware kernel operation. e) Schematic illustration of the neural network for classification and recognition. f) The recognition rate of the neural network evaluated with and without hardware kernels.

different hardware kernels have the function of extracting different vital features.^[63] In this case, the 9 PPC and 9 NPC devices construct their own arrays, respectively. Furthermore, one PPC device is corresponded to one NPC device, while the devices' conductance can be modulated with irradiation power densities and wavelengths. Each pair of the photosynaptic devices was input through a corresponding voltage.^[64] According to Kirchhoff's law, the final output current (I_{output}) is the sum of the PPC device's current and the NPC device's current. This way, a hardware convolution kernel array is formed successfully, where a pair of positive and negative photoconductive devices is considered a complete device. Therefore, both "On"-response and "Off"-response can exist in one kernel array, as presented in Figure 6b. Also, Figure 6c demonstrates the function of visual processing based on the hardware kernel, including extracting the key features of the image and experimental details found

in Figure S28 (Supporting Information). As a demonstration, three different hardware kernels are used in visual processing here. We can then achieve three different ways of processing images by modulating specific conductance values for each device with varying irradiation wavelengths. In this case, it is possible to map the reverse, edge, and embossing of the convolution kernels (3×3) to the hardware kernel array.^[65] The experimental results of the hardware kernel operation are in good agreement with the software simulation results, which reproduce the image features as shown in Figure 6d. It is noted that the experimental results were extracted from the photo-response data of the InGaAs/PC₆₁BM and InGaAs/C8-BTBT devices. In addition, the experimental results of the edge and embossing reveal that the image features can be more colorful due to the difference in the conductance amplitude between two different devices in the hardware kernel.

After that, we input the features detected by the hardware kernel (constructed from devices with tunable conductivities) into the neural network for classification and recognition to evaluate the neural network's performance. The dataset is made of 6 color figures (3×3 pixels) containing the two letters of "V" and "L" in red (R), green (G), and blue (B), respectively.^[66] In this work, the image input signals are defined as 0.8 V to 1 V (for R), 0.4 V to 0.6 V (for G), and 0.1 V to 0.3 V (for B).^[23] This way, we can randomly generate images based on this definition. The 250 images are arbitrarily generated from each of the 6 color figures. Therefore, 1200 images are employed as a training set for learning, while 300 images are used as a test set to evaluate classification accuracy. Figure 6e shows the key feature values of the image as the input signals of the neural network through 9 hardware kernels, which are composed of 3 red, 3 green, and 3 blue light conductance hardware kernels. Moreover, all hardware kernels possess reverse, edge, and embossing features. Therefore, the single-layer-perceptron neural network consists of 9 input and 6 output neurons. The recognition rate of the neural network is then evaluated with and without hardware kernels, respectively (Figure 6f). Impressively, the recognition rate with hardware kernels reaches 100%; in comparison, only $\approx 51\%$ is obtained without hardware kernels, which verifies that the hardware kernel has the ability to detect and classify target features with different colors. In general, since it takes 3 neurons to recognize the color of an image pixel, the 9-pixel image here requires 27 input neurons. The color can be directly differentiated through our hardware kernel. The number of input neurons required by the neural network has changed to 9. Notably, when constructing the artificial hardware neural network, the hardware kernel can greatly reduce the number of input neurons and synaptic weights, thus reducing the complexity and power consumption of the neural network. All these results evidently demonstrate the applicability of the hardware kernel constructed by two different kinds of devices (i.e., InGaAs/C8-BTBT and InGaAs/PC₆₁BM) with tunable photoconductivities for artificial visual systems.

3. Conclusion

In conclusion, the artificial photosynaptic device arrays are successfully configured with the InGaAs NW arrays top-wrapped with the organic semiconductor thin films of C8-BTBT or PC₆₁BM to realize persistent NPC or PPC phenomena, respectively. The two type-I heterojunctions (i.e., InGaAs/C8-BTBT and InGaAs/PC₆₁BM) can effectively mimic the essential synaptic visual behaviors, such as PPF and EPSC, based on their different photoconductivities. In order to demonstrate the large-scale processability of printable NW arrays and solution-processed organic thin films, 4×4 artificial photosynaptic device arrays are fabricated, exhibiting reliable optical memory functions when applying different gate voltages. More importantly, utilizing these two different photosynaptic devices with negative and positive photoconductivities, the hardware kernel can be constructed for simulating the visual processing and recognition of the human eye. Due to the tunable photoconductivity and response to different irradiation

wavelengths, an efficient neural network with 100% classification accuracy is achieved. All these results evidently indicate the promising potential of artificial photosynaptic devices based on organic molecule-nanowire heterojunctions for practical utilization in artificial visual systems.

4. Experimental Section

Nanowire Synthesis: InGaAs nanowires were synthesized on SiO₂/Si wafer pieces (50 nm thick thermally grown oxide) in a two-zone horizontal tube furnace using a chemical vapor transport method. The mixed InAs and GaAs powders (with a ratio of 1:9 in wt.%) were loaded into a boron nitride crucible placed at the upstream zone of the furnace. The growth substrate pre-deposited with a 0.5 nm thick (nominal thickness) Au film as the catalyst was set at the downstream zone. The temperature of the downstream zone was first elevated to 800 °C and kept for 10 min in order to anneal the Au catalyst. Then, the temperature of the downstream zone was cooled directly to the growth temperature (660 °C) for the first step of growth, and the source temperature started to elevate simultaneously. When the source temperature reached the designated value (820 °C), the first nucleation step began. After 1–2 min, the downstream was stopped with the heating and then cooled to a second-step growth temperature (580 °C). Finally, the second step of growth lasted for 40 min. During the entire growth process, hydrogen (99.9995%) was used as a carrier gas, with the flowrate maintained at 100 sccm.

Photosynaptic Devices Fabrication and Characterization: The well-developed contact printing technique was adopted to fabricate NW parallel arrays on the highly boron-doped p-type Si substrates with a 50 nm thick thermally grown gate oxide.^[67,68] Photolithography was utilized to define the source and drain regions, while 50 nm thick Ni was thermally deposited as the top electrodes, followed by the lift-off process. The C8-BTBT and PC₆₁BM were dissolved in chlorobenzene with concentrations of 20 mg ml⁻¹ and 25 mg ml⁻¹, respectively. The spin-coating method was utilized to fabricate top-wrapped C8-BTBT film with 2000 rpm per 30 s. After the spin-coating process, the film was annealed at 100 °C for 5 min. The PC₆₁BM organic film was fabricated by the same spin-coating method with 1800 rpm per 30 s, followed by annealing at 60 °C for 5 min. The electrical performance of the FETs was then characterized with a standard electrical probe station and an Agilent 4155C semiconductor analyzer (Agilent Technologies, Santa Clara, CA). The morphologies and EDS mapping of as-prepared NWs were examined using scanning electron microscopy (SEM, Quanta 450 FEG, FEI) and high-resolution transmission electron microscopy (HRTEM, Thermo Scientific, Talos F200X). The morphologies of organic films were evaluated by AFM (Bruker Dimension Icon AFM). The band structure of NWs was investigated by UPS (ThermoFisher, ESCALAB 250Xi). The charge transfer process was characterized by PL and time-resolved PL (FLS980).

Supporting Information

Supporting Information is available from the Wiley Online Library or from the author.

Acknowledgements

P.X. and X.C. contributed equally to this work. The authors acknowledge the RGC Research Fellow Scheme (RFS2021-1S04) and the Theme-based Research (T42-103/16-N) of the Research Grants Council of Hong Kong SAR, China, as well as the Foshan Innovative and Entrepreneurial Research Team Program (NO. 2018IT100031).

Conflict of Interest

The authors declare no conflict of interest.

Data Availability Statement

The data that support the findings of this study are available from the corresponding author upon reasonable request.

Keywords

artificial visual systems, InGaAs, nanowires, negative photoconductivity, organic semiconductors

Received: August 7, 2022

Revised: November 2, 2022

Published online: December 1, 2022

- [1] Z. Zhang, S. Wang, C. Liu, R. Xie, W. Hu, P. Zhou, *Nat. Nanotechnol.* **2021**, *17*, 27.
- [2] I. Sanchez Esqueda, X. Yan, C. Rutherglen, A. Kane, T. Cain, P. Marsh, Q. Liu, K. Galatsis, H. Wang, C. Zhou, *ACS Nano* **2018**, *12*, 7352.
- [3] M.-K. Kim, I.-J. Kim, J.-S. Lee, *Sci. Adv.* **2021**, *7*, 1341.
- [4] K. Roy, A. Jaiswal, P. Panda, *Nature* **2019**, 575, 607.
- [5] L. F. Abbott, W. G. Regehr, *Nature* **2004**, 431, 796.
- [6] Q. Liu, S. Gao, L. Xu, W. Yue, C. Zhang, H. Kan, Y. Li, G. Shen, *Chem. Soc. Rev.* **2022**, *51*, 3341.
- [7] L. Gu, S. Poddar, Y. Lin, Z. Long, D. Zhang, Q. Zhang, L. Shu, X. Qiu, M. Kam, A. Javey, Z. Fan, *Nature* **2020**, 581, 278.
- [8] V. K. Sangwan, M. C. Hersam, *Nat. Nanotechnol.* **2020**, *15*, 517.
- [9] L.-Q. Tao, H. Tian, Y. Liu, Z.-Y. Ju, Y. Pang, Y.-Q. Chen, D.-Y. Wang, X.-G. Tian, J.-C. Yan, N.-Q. Deng, Y. Yang, T.-L. Ren, *Nat. Commun.* **2017**, *8*, 14579.
- [10] M. Wang, Y. Luo, T. Wang, C. Wan, L. Pan, S. Pan, K. He, A. Neo, X. Chen, *Adv. Mater.* **2021**, *33*, 2003014.
- [11] J. Xue, Z. Zhu, X. Xu, Y. Gu, S. Wang, L. Xu, Y. Zou, J. Song, H. Zeng, Q. Chen, *Nano Lett.* **2018**, *18*, 7628.
- [12] S. Gao, G. Liu, H. Yang, C. Hu, Q. Chen, G. Gong, W. Xue, X. Yi, J. Shang, R.-W. Li, *ACS Nano* **2019**, *13*, 2634.
- [13] F. Guo, M. Song, M.-C. Wong, R. Ding, W. F. Io, S.-Y. Pang, W. Jie, J. Hao, *Adv. Funct. Mater.* **2022**, *32*, 2108014.
- [14] L. Q. Zhu, C. J. Wan, L. Q. Guo, Y. Shi, Q. Wan, *Nat. Commun.* **2014**, *5*, 3158.
- [15] S. Lee, R. Peng, C. Wu, M. Li, *Nat. Commun.* **2022**, *13*, 1485.
- [16] Y. Chen, W. Qiu, X. Wang, W. Liu, J. Wang, G. Dai, Y. Yuan, Y. Gao, J. Sun, *Nano. Energy* **2019**, *62*, 393.
- [17] W. Qiu, Y. Huang, L.-A. Kong, Y. Chen, W. Liu, Z. Wang, J. Sun, Q. Wan, J. H. Cho, J. Yang, Y. Gao, *Adv. Funct. Mater.* **2020**, *30*, 2002325.
- [18] J.-L. Meng, T.-Y. Wang, L. Chen, Q.-Q. Sun, H. Zhu, L. Ji, S.-J. Ding, W.-Z. Bao, P. Zhou, D. W. Zhang, *Nano Energy* **2021**, *83*, 105815.
- [19] Q. Shi, D. Liu, D. Hao, J. Zhang, L. Tian, L. Xiong, J. Huang, *Nano Energy* **2021**, *87*, 106197.
- [20] J.-Y. Wu, Y. T. Chun, S. Li, T. Zhang, J. Wang, P. K. Shrestha, D. Chu, *Adv. Mater.* **2018**, *30*, 1705880.
- [21] X. Huang, Q. Li, W. Shi, K. Liu, Y. Zhang, Y. Liu, X. Wei, Z. Zhao, Y. Guo, Y. Liu, *Small* **2021**, 2102820.
- [22] Y. Wang, E. Liu, A. Gao, T. Cao, M. Long, C. Pan, L. Zhang, J. Zeng, C. Wang, W. Hu, S.-J. Liang, F. Miao, *ACS Nano* **2018**, *12*, 9513.
- [23] S. Seo, S.-H. Jo, S. Kim, J. Shim, S. Oh, J.-H. Kim, K. Heo, J.-W. Choi, C. Choi, S. Oh, D. Kuzum, H. S. P. Wong, J.-H. Park, *Nat. Commun.* **2018**, *9*, 5106.
- [24] Z.-x. Yang, N. Han, M. Fang, H. Lin, H.-Y. Cheung, S. Yip, E.-J. Wang, T. Hung, C.-Y. Wong, J. C. Ho, *Nat. Commun.* **2014**, *5*, 5249.
- [25] D. Li, C. Lan, A. Manikandan, S. Yip, Z. Zhou, X. Liang, L. Shu, Y.-L. Chueh, N. Han, J. C. Ho, *Nat. Commun.* **2019**, *10*, 1664.
- [26] S. Ham, M. Kang, S. Jang, J. Jang, S. Choi, T.-W. Kim, G. Wang, *Sci. Adv.* **2020**, *6*, 1178.
- [27] P. Xie, Y. Huang, W. Wang, Y. Meng, Z. Lai, F. Wang, S. Yip, X. Bu, W. Wang, D. Li, J. Sun, J. C. Ho, *Nano Energy* **2022**, *91*, 106654.
- [28] J. J. Hou, N. Han, F. Wang, F. Xiu, S. Yip, A. T. Hui, T. Hung, J. C. Ho, *ACS Nano* **2012**, *6*, 3624.
- [29] D. Li, S. Yip, F. Li, H. Zhang, Y. Meng, X. Bu, X. Kang, C. Lan, C. Liu, J. C. Ho, *Adv. Opt. Mater.* **2020**, 2001201.
- [30] C.-M. Yang, T.-C. Chen, D. Verma, L.-J. Li, B. Liu, W.-H. Chang, C.-S. Lai, *Adv. Funct. Mater.* **2020**, *30*, 2001598.
- [31] Y. Zhu, C. Wu, Z. Xu, Y. Liu, H. Hu, T. Guo, T. W. Kim, Y. Chai, F. Li, *Nano Lett.* **2021**, *21*, 6087.
- [32] J. J. Hou, F. Wang, N. Han, F. Xiu, S. Yip, M. Fang, H. Lin, T. F. Hung, J. C. Ho, *ACS Nano* **2012**, *6*, 9320.
- [33] Y. Meng, C. Lan, F. Li, S. Yip, R. Wei, X. Kang, X. Bu, R. Dong, H. Zhang, J. C. Ho, *ACS Nano* **2019**, *13*, 6060.
- [34] W. Wang, S. Yip, Y. Meng, W. Wang, F. Wang, X. Bu, Z. Lai, X. Kang, P. Xie, Q. Quan, C. Liu, J. C. Ho, *Adv. Opt. Mater.* **2021**, *9*, 2101289.
- [35] P. Xie, T. Liu, J. Sun, J. Yang, *Adv. Funct. Mater.* **2022**, 2200843.
- [36] X. Li, P. Xie, X. Mo, Y. Xiang, Z. Xiao, T. Xionsong, H. Huang, J. Sun, G. Dai, J. Yang, *Phys. Status. solidi-R* **2021**, *15*, 2000479.
- [37] H. Kobayashi, N. Kobayashi, S. Hosoi, N. Koshitani, D. Murakami, R. Shirasawa, Y. Kudo, D. Hobara, Y. Tokita, M. Itabashi, *J. Chem. Phys.* **2013**, *139*, 014707.
- [38] H. Xia, S. Tong, C. Zhang, C. Wang, J. Sun, J. He, J. Zhang, Y. Gao, J. Yang, *Appl. Phys. Lett.* **2018**, *112*, 233301.
- [39] L. Shen, S. Yip, C. Lan, L. Shu, D. Li, Z. Zhou, C.-Y. Wong, E. Y. B. Pun, J. C. Ho, *Adv. Mater. Interfaces* **2018**, *5*, 1701104.
- [40] J. Chen, C. H. Yang, R. A. Wilson, M. J. Yang, *Appl. Phys. Lett.* **1992**, *60*, 2113.
- [41] N. Guo, W. Hu, L. Liao, S. Yip, J. C. Ho, J. Miao, Z. Zhang, J. Zou, T. Jiang, S. Wu, X. Chen, W. Lu, *Adv. Mater.* **2014**, *26*, 8203.
- [42] Y. Han, M. Fu, Z. Tang, X. Zheng, X. Ji, X. Wang, W. Lin, T. Yang, Q. Chen, *ACS Appl. Mater. Interfaces* **2017**, *9*, 2867.
- [43] M. Zhang, Z. Tang, X. Liu, J. Van der Spiegel, *Nat. Electron.* **2020**, *3*, 191.
- [44] H.-L. Park, Y. Lee, N. Kim, D.-G. Seo, G.-T. Go, T.-W. Lee, *Adv. Mater.* **2020**, *32*, 1903558.
- [45] S. Dai, X. Wu, D. Liu, Y. Chu, K. Wang, B. Yang, J. Huang, *ACS Appl. Mater. Interfaces* **2018**, *10*, 21472.
- [46] C. Han, X. Han, J. Han, M. He, S. Peng, C. Zhang, X. Liu, J. Gou, J. Wang, *Adv. Funct. Mater.* **2022**, 2113053.
- [47] C. Fan, X. Xu, K. Yang, F. Jiang, S. Wang, Q. Zhang, *Adv. Mater.* **2018**, *30*, 1804707.
- [48] W. Eaton Samuel, M. Lai, A. Gibson Natalie, B. Wong Andrew, L. Dou, J. Ma, L.-W. Wang, R. Leone Stephen, P. Yang, *P. Natl. A. Sci* **2016**, *113*, 1993.
- [49] Y. Zhao, X. Liu, G. Feng, L. Lyu, L. Li, S. Wang, J. Jiang, Y. Li, D. Niu, H. Xie, Y. Gao, *Results. Phys* **2020**, *19*, 103590.
- [50] H. Xie, D. Niu, Y. Zhao, S. Wang, B. Liu, Y. Liu, H. Huang, P. Wang, D. Wu, Y. Gao, *Synthetic. Met* **2020**, *260*, 116261.
- [51] D. Yang, X. Zhang, K. Wang, C. Wu, R. Yang, Y. Hou, Y. Jiang, S. Liu, S. Priya, *Nano Lett.* **2019**, *19*, 3313.

- [52] J. Han, J. Wang, M. Yang, X. Kong, X. Chen, Z. Huang, H. Guo, J. Gou, S. Tao, Z. Liu, Z. Wu, Y. Jiang, X. Wang, *Adv. Mater.* **2018**, *30*, 1804020.
- [53] C.-H. Chiang, C.-G. Wu, *Nat. Photonics* **2016**, *10*, 196.
- [54] S. Foster, F. Deledalle, A. Mitani, T. Kimura, K.-B. Kim, T. Okachi, T. Kirchartz, J. Oguma, K. Miyake, J. R. Durrant, S. Doi, J. Nelson, *Adv. Energy Mater.* **2014**, *4*, 1400311.
- [55] Z. Ahmad, M. Awais, M. A. Najeeb, R. A. Shakoor, F. Touati, *Springer International Publishing Cham* **2017**, 95.
- [56] A. S. Shikoh, Z. Ahmad, F. Touati, R. A. Shakoor, J. Bhadra, N. J. Al-Thani, *RSC Adv.* **2017**, *7*, 35445.
- [57] F.-C. Wu, P.-R. Li, B.-R. Lin, R.-J. Wu, H.-L. Cheng, W.-Y. Chou, *ACS. Appl. Mater. Interfaces* **2021**, *13*, 45822.
- [58] T. Chang, S.-H. Jo, W. Lu, *ACS Nano* **2011**, *5*, 7669.
- [59] L. Wu, A. Wang, J. Shi, J. Yan, Z. Zhou, C. Bian, J. Ma, R. Ma, H. Liu, J. Chen, Y. Huang, W. Zhou, L. Bao, M. Ouyang, S. J. Pennycook, S. T. Pantelides, H.-J. Gao, *Nat. Nanotechnol.* **2021**, *16*, 882.
- [60] J. Meng, T. Wang, Z. He, Q. Li, H. Zhu, L. Ji, L. Chen, Q. Sun, D. W. Zhang, *Nano Res.* **2021**, *15*, 2472.
- [61] Y. Meng, F. Li, C. Lan, X. Bu, X. Kang, R. Wei, S. Yip, D. Li, F. Wang, T. Takahashi, T. Hosomi, K. Nagashima, T. Yanagida, J. C. Ho, *Sci. Adv.* **2020**, *6*, 6389.
- [62] S. Hong, H. Cho, B. H. Kang, K. Park, D. Akinwande, H. J. Kim, S. Kim, *ACS Nano* **2021**, *15*, 15362.
- [63] C.-Y. Wang, S.-J. Liang, S. Wang, P. Wang, Z. a. Li, Z. Wang, A. Gao, C. Pan, C. Liu, J. Liu, H. Yang, X. Liu, W. Song, C. Wang, B. Cheng, X. Wang, K. Chen, Z. Wang, K. Watanabe, T. Taniguchi, J. J. Yang, F. Miao, *Sci. Adv.* **2020**, *6*, 6173.
- [64] P. Yao, H. Wu, B. Gao, J. Tang, Q. Zhang, W. Zhang, J. J. Yang, H. Qian, *Nature* **2020**, *577*, 641.
- [65] H. Jang, C. Liu, H. Hinton, M.-H. Lee, H. Kim, M. Seol, H.-J. Shin, S. Park, D. Ham, *Adv. Mater.* **2020**, *32*, 2002431.
- [66] M. Prezioso, F. Merrikh-Bayat, B. D. Hoskins, G. C. Adam, K. K. Likharev, D. B. Strukov, *Nature* **2015**, *521*, 61.
- [67] Z. Fan, J. C. Ho, Z. A. Jacobson, R. Yerushalmi, R. L. Alley, H. Razavi, A. Javey, *Nano Lett.* **2008**, *8*, 20.
- [68] T. Takahashi, K. Takei, J. C. Ho, Y.-L. Chueh, Z. Fan, A. Javey, *J. Am. Chem. Soc.* **2009**, *131*, 2102.